Experimental Demonstration of Topological Surface States Protected by Time-Reversal Symmetry

Tong Zhang,[1,2] Peng Cheng,[1] Xi Chen,[1,*] Jin-Feng Jia,[1] Xucun Ma,[2] Ke He,[2] Lili Wang,[2] Haijun Zhang,[2] Xi Dai,[2] Zhong Fang,[2] Xincheng Xie,[2] and Qi-Kun Xue[1,2,†]

[1]*Department of Physics, Tsinghua University, Beijing 100084, China*
[2]*Institute of Physics, Chinese Academy of Sciences, Beijing 100080, China*

(Received 20 August 2009; published 23 December 2009)

We report direct imaging of standing waves of the nontrivial surface states of topological insulator Bi_2Te_3 using a scanning tunneling microscope. The interference fringes are caused by the scattering of the topological states off Ag impurities and step edges on the $Bi_2Te_3(111)$ surface. By studying the voltage-dependent standing wave patterns, we determine the energy dispersion $E(k)$, which confirms the Dirac cone structure of the topological states. We further show that, very different from the conventional surface states, backscattering of the topological states by nonmagnetic impurities is completely suppressed. The absence of backscattering is a spectacular manifestation of the time-reversal symmetry, which offers a direct proof of the topological nature of the surface states.

DOI: 10.1103/PhysRevLett.103.266803 PACS numbers: 73.20.−r, 68.37.Ef, 72.10.Fk, 72.25.Dc

The strong spin-orbital coupling in a certain class of materials gives rise to the novel topological insulators in two [1,2] and three dimensions [3–7] in the absence of an external magnetic field. The topological states on the surfaces of three-dimensional (3D) materials have been studied recently in $Bi_{1-x}Sb_x$ [6,8,9], Bi_2Te_3, and Bi_2Se_3 [7,10–13], which possess insulating gaps in the bulk and gapless states on surfaces. The surface states of a 3D topological insulator are comprised of an odd number of massless Dirac cones, and the crossing of two dispersion branches with opposite spins is fully protected by the time-reversal symmetry at the Dirac points. Such spin-helical states are expected to bring forward exotic physics, such as magnetic monopole [14] and Majorana fermions [15,16]. To date, the experimental study of topological insulators is predominantly limited to the determination of their band structure by angle-resolve photoemission spectroscopy (ARPES) [8–13]. Distinct quantum phenomena associated with the nontrivial topological electronic states still remain unexplored. Particularly, there is no direct experimental evidence for the time-reversal symmetry that protects the topological property. Here, using the low temperature scanning tunneling microscopy (STM) and spectroscopy (STS), we report the direct observation of quantum interference caused by scattering of the 2D topologically nontrivial surface states off impurities and surface steps. Our work strongly supports the surface nature of the topological states and provides a way to study the spinor wave function of the topological state. More significantly, we find that the backscattering of topological states by a nonmagnetic impurity is forbidden. This result directly demonstrates that the surface states are indeed quantum mechanically protected by the time-reversal symmetry.

The interference patterns in STM experiments [17–20] result from the 2D surface states perturbed by surface defects. A surface state is uniquely characterized by a 2D Bloch wave vector $\vec{k}$ within the surface Brillouin zone (SBZ). During elastic scattering, a defect scatters the incident wave with a wave vector $\vec{k}_i$ into $\vec{k}_f = \vec{k}_i + \vec{q}$, with $\vec{k}_i$ and $\vec{k}_f$ being on the same constant-energy contour (CEC). The quantum interference between the initial and final states results in a standing wave pattern whose spatial period is given by $2\pi/q$. When the STM images of a

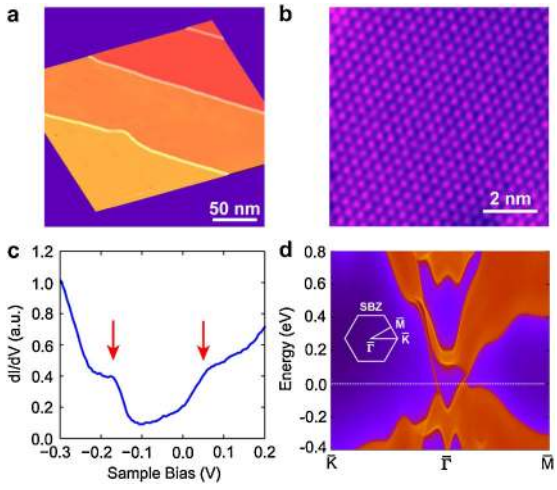

FIG. 1 (color online). (a) The STM topograph (250 nm × 250 nm) of the $Bi_2Te_3(111)$ film. Imaging conditions: $V = 3$ V, $I = 50$ pA. (b) The atomic-resolution image (−40 mV, 0.1 nA). Tellurium atom spacing is about 4.3 Å. (c) dI/dV spectrum taken on bare $Bi_2Te_3(111)$ surface. Set point: $V = 0.3$ V, $I = 0.1$ nA. The arrows indicate the bottom of conduction band (right) and the top of valence band (left), respectively. (d) Calculated band structure of $Bi_2Te_3(111)$ along high-symmetry directions of SBZ (see the inset). The lines around the $\bar{\Gamma}$ point in the energy gap are the surface states.

standing wave are Fourier transformed [21], the scattering wave vector $\vec{q}$ ($\hbar\vec{q}$ is the momentum transfer) becomes directly visible in the reciprocal space. In contrast, for bulk states, there will be continuous ranges of wave vectors on the projected SBZ for a given energy. Usually, no distinct interference fringe can be produced by bulk states and visualized by STM. In this sense, the standing wave is surface states sensitive and particularly suitable for studying topological insulators.

Our experiments were conducted in an ultrahigh vacuum low temperature (down to 0.4 K) STM system equipped with molecular beam epitaxy (MBE) for film growth (Unisoku). The stoichiometric Bi_2Te_3 film was prepared on single crystal substrate Si(111) by MBE. Details of sample preparation are described elsewhere [22]. Shown in Fig. 1(a) is a typical STM image of the Bi_2Te_3 film with a thickness of $\sim$100 nm. The atomically flat morphology of the film is clearly observed. The three steps seen in Fig. 1(a) all have the height (0.94 nm) of a quintuple layer. The steps are preferentially oriented along the three close-packing ([100], [110], and [010]) directions. The image with atomic resolution [Fig. 1(b)] exhibits the two-dimensional hexagonal lattice structure of the Te-terminated (111) surface of Bi_2Te_3. Our STM observation reveals a small density of clover-shaped defects on the surface (see supporting material in [23]). Similar to Bi_2Se_3 [13,24,25], these structures can be assigned to the substitutional Bi defects at the Te sites by examining their registration with respect to the (1×1)-Te lattice in the topmost layer.

The surface states of Bi_2Te_3 were investigated by STS and the first-principles calculations [7]. The STS detects the differential tunneling conductance dI/dV [Fig. 1(c)], which gives a measure of the local density of states (LDOS) of electrons at energy eV. The Fermi level (zero bias) is within the energy gap, indicating that the film is an intrinsic bulk insulator [22]. The differential conductance in the bulk insulating gap linearly depends on the bias and is attributed to the gapless surface states. These features in STS are in good agreement with those obtained by the first-principles calculations (see supporting material in [23]). According to the calculations [Fig. 1(d)], the topological states of Bi_2Te_3 form a single Dirac cone at the center ($\bar{\Gamma}$ point) of the SBZ [10,11], giving rise to a vanishing DOS in the vicinity of $k = 0$. However, the surface states around the $\bar{\Gamma}$ point overlap in energy with the bulk valence band. For this reason, the Dirac point is invisible in STS.

On the aforementioned surface, we deposited a small amount (0.01 ML) of Ag atoms, which form trimmers on the surface, as shown in Fig. 2(a) and more clearly in the supporting material [23]. The atomically resolved STM image (see supporting material in [23]) reveals that the Ag atom in a trimmer adsorbs on the top site of a surface Te atom [26]. This situation is schematically shown in Fig. 2(b). In addition, the Fermi level shifts upwards in energy by 20–30 meV after Ag deposition, suggesting electron transfer from the Ag atoms to the substrate. The dI/dV mapping was then carried out in a region containing Ag trimmers. At each data point, the feedback was turned off and the bias modulation was turned on to record dI/dV. This procedure resulted in a series of spatial mapping of LDOS at various bias voltages.

Figures 2(c)–2(g) summarize the dI/dV maps for bias voltages ranging from 50 to 400 mV from the area shown in Fig. 2(a). The first striking aspect of these images is the existence of standing wave [17–19] in the vicinity of the Ag trimmers. The spatial modulation of LDOS by an Ag trimmer forms a hexagonal pattern whose edges are perpendicular to the $\bar{\Gamma}$-$\bar{M}$ directions in SBZ. This situation is more clearly resolved at large bias voltages [Figs. 2(f) and 2(g)]. As expected, the interference pattern is anisotropic as a result of the hexagram CEC [10]. The spatial period of the standing wave scales inversely with the bias voltage and is determined by the momentum transfer during scat-

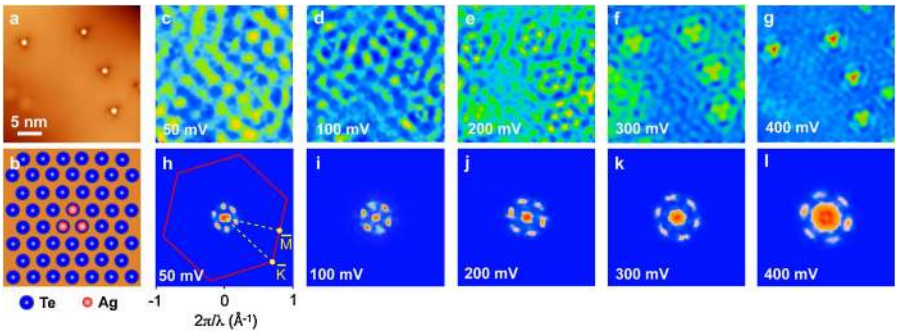

FIG. 2 (color online). Standing waves induced by Ag trimmers on $Bi_2Te_3(111)$ surface. (a) STM image (28 nm $\times$ 28 nm) of a region with four Ag trimmers adsorbed on $Bi_2Te_3(111)$ surface. (b) The adsorption geometry of Ag trimmer. (c)–(g) The dI/dV maps of the same area as (a) at various sample bias voltages. The current was set at 0.1 nA. Each map has 128×128 pixels and took 2 h to complete. The interference fringes are evident in the images. (h)–(k) The FFT power spectra of the dI/dV maps in (c)–(g). The SBZ in (h) is superimposed on the power spectra to indicate the directions in $\vec{q}$ space. The resolution of FFT, which is $2\pi/28$ nm^{-1}, is determined by the size of the STM image.

tering at a given energy. Below 50 meV, the fringes become obscured. It results from a combination of two effects: (i) the wavelength increases rapidly as the bias voltage approaches the Dirac point, where $k = 0$; (ii) at low energy, CEC becomes more isotropic and more topological surface states with different wavelengths are involved in the formation of standing wave as indicated by the first-principles calculations [Fig. 1(d)]. The superposition of waves with various wavelengths smears out the interference fringes. With increasing bias, especially after the surface states in the $\bar{\Gamma}$-$\bar{M}$ direction merge into the bulk conduction band at ~0.2 eV above the Dirac point according to calculation [Fig. 1(d)], the contribution of states in the $\bar{\Gamma}$-$\bar{M}$ direction vanishes and the states in the vicinity of $\bar{\Gamma}$-$\bar{K}$ direction gradually gain more weight, leading to more distinct interference patterns. After the surface states in the $\bar{\Gamma}$-$\bar{K}$ direction merge into the bulk conduction band at ~0.6 eV above the Dirac point [Fig. 1(d)], the standing waves fade out again.

To quantify the standing waves and obtain the scattering wave vectors, we performed fast Fourier transformation (FFT) of the dI/dV maps into the $\vec{q}$ space [Figs. 2(h)–2(l)]. One important feature in the power spectra can be immediately discerned by comparing the sixfold symmetric pattern in the $\vec{q}$ space with SBZ [the (red) hexagon in Fig. 2(h)]: the regions with high intensity are always oriented toward the $\bar{\Gamma}$-$\bar{M}$ directions, while the intensity in the $\bar{\Gamma}$-$\bar{K}$ directions vanishes (see supporting material in [23]). Such phenomena can be understood by exploring possible scattering processes on the CEC in the reciprocal space [Fig. 3(a)]. Generally, the $\vec{k}_i$ and $\vec{k}_f$ pairs with high joint DOS should dominate the quantum interference. For energies at which the interference fringes are prominent, the regions on CEC with high DOS are primarily centered around the $\bar{\Gamma}$-$\bar{K}$ directions [10]. Therefore, three scattering wave vectors, labeled $\vec{q}_1$, $\vec{q}_2$, and $\vec{q}_3$, might be expected to appear in the power spectra. Among them, however, only $\vec{q}_2$ is along the $\bar{\Gamma}$-$\bar{M}$ directions and can generate the observed standing waves. Both $\vec{q}_1$ and $\vec{q}_3$ are invisible in the power spectra. There is a simple argument to account for the disappearance of $\vec{q}_1$: the time-reversal invariance. The topological states $|\vec{k}\uparrow\rangle$ and $|-\vec{k}\downarrow\rangle$ are related by the time-reversal transformation: $|-\vec{k}\downarrow\rangle = \mathcal{T}|\vec{k}\uparrow\rangle$, where $\mathcal{T}$ is the time-reversal operator. It is straightforward to show that $\langle -\vec{k}\downarrow|U|\vec{k}\uparrow\rangle = -\langle\vec{k}\uparrow|U|-\vec{k}\downarrow\rangle^* = -\langle -\vec{k}\downarrow|U|\vec{k}\uparrow\rangle = 0$ for fermions, where U is a time-reversal invariant operator and represents the impurity potential of the nonmagnetic Ag impurity. Therefore, the backscattering between $\vec{k}$ and $-\vec{k}$ is quantum mechanically prohibited. Most of the observed features in the interference pattern, including the extinction of wave vector $\vec{q}_3$, have been recently well explained by a theoretical treatment [27] based on the T-matrix approach for multiband systems [28]. However, other factors, for example, the underlying geometry and the electronic structure of the scattering centers, may play roles in the formation of standing waves. Further theoretical and experimental study is needed to fully understand the interference pattern.

We can obtain the dispersion of the massless Dirac fermions in the $\bar{\Gamma}$-$\bar{K}$ direction using the interference patterns and their Fourier transforms. For $\vec{q}_2$, the scattering geometry determines $q_2 = \sqrt{3}k$ [see Fig. 3(a)], where k is the wave vector in the $\bar{\Gamma}$-$\bar{K}$ direction at a given energy. The resulting k values vary linearly with energy [Fig. 3(b)]. The slope of the linear fitting provides a measurement of the

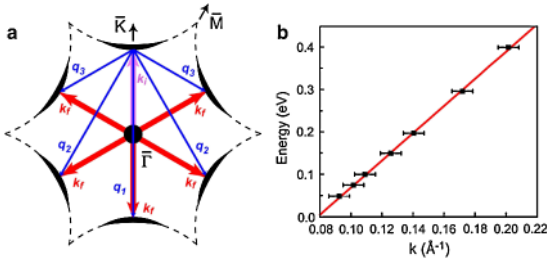

FIG. 3 (color online). (a) The scattering geometry. The CEC is in the shape of a hexagram. The dominant scattering wave vectors connect two points in $\bar{\Gamma}$-$\bar{K}$ directions on CEC. $\vec{k}_i$ and $\vec{k}_f$ denote the wave vectors of incident and scattered states. $\vec{q}_1$, $\vec{q}_2$, and $\vec{q}_3$ are three possible scattering wave vectors. (b) Energy dispersion as a function of k in the $\bar{\Gamma}$-$\bar{K}$ direction. The data are derived from FFT in Fig. 2. The line shows a linear fit to the data with $v_F = 4.8 \times 10^5$ m/s. The error bars represent the resolution of FFT (see the caption of Fig. 2).

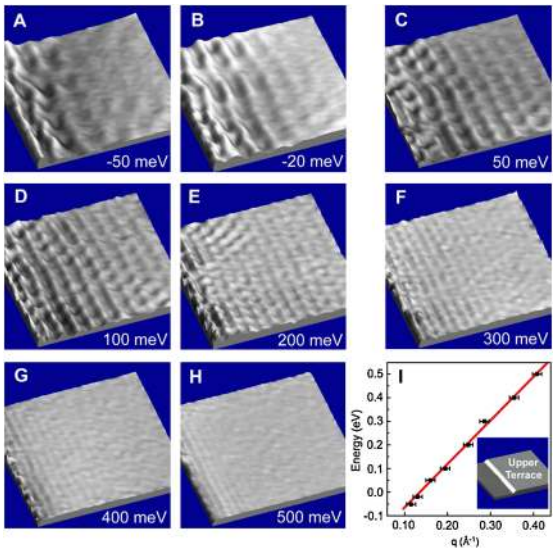

FIG. 4 (color online). Standing waves on the upper terrace by a step edge [(a)–(h)]. All of the images are dI/dV maps at various bias voltages of an area of 35 × 35 nm. Imaging conditions: I = 0.1 nA. (i) Energy dispersion deduced from the standing waves at the step edge. The dispersion is a function of the scattering wave vector q. The inserted STM image shows the step that produces the standing waves in (a)–(h).

Dirac fermion velocity v_F, which is 4.8×10^5 m/s. In addition, the energy of the Dirac point is estimated to be 0.25 eV by the intercept of the dispersion with the energy axis. These observations are in agreement with the results from the first-principles calculation and the ARPES data [7,22]. More importantly, the unoccupied states, which are inaccessible to ARPES, can be probed by the standing waves with STM.

Interference fringes are also found at the step edges on the surface [29] [Figs. 4(a)–4(h)]. Similar to the case of Ag trimmers, the standing waves produced by steps are predominantly propagating along the $\bar{\Gamma}$-$\bar{M}$ direction. The fringes are clearly visible even at the negative bias voltages probably owing to the stronger scattering potential compared to that of the Ag trimmers. The dispersion curve deduced from these patterns again shows a linear relation between the scattering wave vector and the energy [Fig. 4(i)]. Using the slope of the linear fitting together with the same scattering geometry as that for the Ag trimmer, the Fermi velocity is found to be 4.8×10^5 m/s again.

The existence of standing waves strongly supports the surface nature of topological states. Furthermore, the absence of backscattering makes the topological standing waves more extraordinary as compared to the conventional surface states on metal samples [17–20]. An important issue that immediately arises is whether the topological states respond differently to the magnetic and the nonmagnetic impurities. Theoretically, it was pointed out [5,30,31] that a time-reversal breaking perturbation, such as magnetic impurities, can induce scattering between the states $|\vec{k}\uparrow\rangle$ and $-|\vec{k}\downarrow\rangle$ and open up a local energy gap at the Dirac point. It remains an open question to observe the distinct signature of time-reversal breaking in topological insulators.

We thank S.-C. Zhang, X.-L. Qi, Y. Ran, and S.-Q. Shen for valuable discussions. The work is supported by NSFC and the National Basic Research Program of China. The STM topographic images were processed using WSXM (www.nanotec.es).

Note added.—At the completion of this manuscript for submission, we became aware of related work by P. Roushan *et al.* [32]. The authors reported STM study of scattering from disorder in BiSb alloy.

*xc@mail.tsinghua.edu.cn
†qkxue@mail.tsinghua.edu.cn

[1] B. A. Bernevig, T. L. Hughes, and S.-C. Zhang, Science **314**, 1757 (2006).
[2] M. König *et al.*, Science **318**, 766 (2007).
[3] L. Fu, C. L. Kane, and E. J. Mele, Phys. Rev. Lett. **98**, 106803 (2007).
[4] J. E. Moore and L. Balents, Phys. Rev. B **75**, 121306(R) (2007).
[5] X.-L. Qi, T. L. Hughes, and S.-C. Zhang, Phys. Rev. B **78**, 195424 (2008).
[6] J. C. Y. Teo, L. Fu, and C. L. Kane, Phys. Rev. B **78**, 045426 (2008).
[7] H. J. Zhang *et al.*, Nature Phys. **5**, 438 (2009).
[8] D. Hsieh *et al.*, Nature (London) **452**, 970 (2008).
[9] D. Hsieh *et al.*, Science **323**, 919 (2009).
[10] Y. L. Chen *et al.*, Science **325**, 178 (2009).
[11] D. Hsieh *et al.*, Nature (London) **460**, 1101 (2009).
[12] Y. Xia *et al.*, Nature Phys. **5**, 398 (2009).
[13] Y. S. Hor *et al.*, Phys. Rev. B **79**, 195208 (2009).
[14] X.-L. Qi, R. Li, J. Zang, and S.-C. Zhang, Science **323**, 1184 (2009).
[15] L. Fu and C. L. Kane, Phys. Rev. Lett. **100**, 096407 (2008).
[16] X.-L. Qi, T. L. Hughes, S. Raghu, and S.-C. Zhang, Phys. Rev. Lett. **102**, 187001 (2009).
[17] M. F. Crommie, C. P. Lutz, and D. M. Eigler, Nature (London) **363**, 524 (1993).
[18] M. F. Crommie, C. P. Lutz, and D. M. Eigler, Science **262**, 218 (1993).
[19] Y. Hasegawa and Ph. Avouris, Phys. Rev. Lett. **71**, 1071 (1993).
[20] G. A. Fiete and E. J. Heller, Rev. Mod. Phys. **75**, 933 (2003).
[21] J. E. Hoffman *et al.*, Science **297**, 1148 (2002).
[22] Y. Y. Li *et al.* (unpublished).
[23] See EPAPS Document No. E-PRLTAO-103-178952 for additional materials about the experimental results. For more information on EPAPS, see http://www.aip.org/pubservs/epaps.html.
[24] S. Urazhdin *et al.*, Phys. Rev. B **66**, 161306(R) (2002).
[25] S. Urazhdin *et al.*, Phys. Rev. B **69**, 085313 (2004).
[26] There are another two candidate models for the Ag defects: the Ag atoms can either substitute the topmost layer Te atoms or the second layer Bi atoms. In the latter case, one Ag atom is enough to produce the observed triangular shape image. This model is supported by the fact that all of the trimmerlike features are oriented along the same direction. Although the exact structure of Ag defect does not affect the main conclusion here, it remains an interesting subject for further study. In addition, the shape of the scattering center does not influence the interference pattern when the wavelength of the standing wave is much larger than the dimension of the defect.
[27] W.-C. Lee, C. J. Wu, D. P. Arovas, and S.-C. Zhang, arXiv:0910.1668.
[28] W.-C. Lee and C. J. Wu, Phys. Rev. Lett. **103**, 176101 (2009).
[29] Z. Alpichshev *et al.*, arXiv:0908.0371.
[30] Q. Liu, C.-X. Liu, C. Xu, X.-L. Qi, and S.-C. Zhang, Phys. Rev. Lett. **102**, 156603 (2009).
[31] X.-L. Qi, T. L. Hughes, and S.-C. Zhang, Nature Phys. **4**, 273 (2008).
[32] P. Roushan *et al.*, Nature (London) **460**, 1106 (2009).